Aeroelastic Load Control of Large and Flexible Wind Turbines through Mechanically Driven Flaps

Xing Wei [1], Bing Feng Ng[2], Xiaowei Zhao[1,*]

[1] ***School of Engineering, University of Warwick, Coventry CV4 7AL, United Kingdom***

[2] ***School of Mechanical and Aerospace Engineering, Nanyang Technological University, Singapore 639798***

Abstract

The load reduction of the wind turbine through the use of flaps actuated through novel mechanical network is studied. The aeroservoelastic model of the wind turbine couples the composite beam description for blades and tower to the unsteady vortex-lattice method for the aerodynamics. The trailing-edge flap dynamics are incorporated to the wind turbine model to enable the use of mechanical network to control the flap rotation. A passive mechanical controller is proposed, which senses the relative angular velocity of the trailing-edge flap and generate the control torque. The mechanical controller is realized by passive components including springs, dampers and inerters in rotational form. The parameters of the mechanical components and flap configuration parameters are optimised by H_∞ and H_2 optimisation, respectively. It is shown that mechanical controllers exhibit marked reductions in blade root-bending moment, blade tip deflection and tower top fore-aft deflection in the presence of external disturbances, especially with the optimised flap configuration parameters.

Keywords: Aeroelastic load control, mechanical network controller, inerter, H_∞ optimisation, H_2 optimization

*corresponding author

Email address: Xiaowei.Zhao@warwick.ac.uk (Xiaowei Zhao)

1. Introduction

Wind power is a fast growing source of green energy with continued efforts on reducing its cost. Increasing the size of wind turbines has been adopted extensively to achieve this aim. The ever increasing size of wind turbine blades lead to the increase in their flexibility, which can cause structural degradation and fatigue failure in extreme flow conditions [1]. Thus, reducing the load experienced by flexible blades has become the primary research objective to prolong the service life of the wind turbines. Load reduction on blades not only lowers its own cost, but also leads to reduced loads in other components such as drive train and tower, thereby curbing maintenance cost [2].

Wind turbines are subject to significant and rapid fluctuating loads, which arise from a variety of sources including inflow turbulence, tower shadow, wind shear and yawed flow conditions [2]. The ever increasing size of wind turbine blades not only adds gravitational effects to blade fatigue, but also causes larger wind speed variations across the rotor disk, which enhances the difficulty of mitigating aerodynamic loads [3].

Several control methods have been applied to reduce aerodynamic loads on wind turbine blades, which can be classified into passive and active methods. The most traditional and simple passive control method, stall control, has been extensively used on modern wind turbines for power regulation. However, stall-induced vibrations is unavoidable. Herencia et al. [4] designed the morphing wing by employing the aeroelastic tailoring. Taking advantage of the anisotropic properties of composites, morphing wings are capable of modifying its shape to avoid excessive loadings by passive actuation [5]. The flexural anisotropy properties enable the morphing wing to twist under bending loads. However, for wind turbine applications, such systems are not necessarily reliable and easily maintainable [6]. Besides passive control methods, pitch control is the most widely studied active control method that alters the aerodynamic properties of the blades (change of angle-of-attack or lift coefficient) [6, 7]. Bossanyi [8] designed the individual pitch controller based on measurements of the asymmetric loading. However, pitch control is unable to completely mitigate blade loads for large blades as local wind profile varies significantly along the blade and it is too slow to handle fast turbulence. Moreover, fast and excessive use of blade pitch will results in wear and tear of the pitch bearings and actuators. Actually, pitch actuator failure is one of the major reasons for turbine downtime. Consequently, a more advanced and innovative concept termed "smart rotor control" has been proposed to achieve faster and detailed load reduction of wind turbine blades [9, 10].

As a term derived from rotorcraft research, smart rotor refers to blades that are equipped with distributed control surfaces that can be actuated rapidly for localised

load reductions. The aerodynamic surfaces include trailing-edge flaps and microtabs, among which the former has been widely studied. Successful wind tunnel experiment of small scaled wind turbine equipped with smart rotor has demonstrated the effectiveness on mitigating loads by actively controlled trailing-edge flap [10]. Several control schemes, such as MPC [11], H_∞ [12, 13], LQG [14] and LQR [15], have been applied to actively adjust trailing-edge flap angle to react to both deterministic loads (such as wind shear and tower shadow) and stochastic loads (such as gusts) [16]. These control methods, however, are active techniques that require sensors, controllers and actuators, which from the design consideration, could be complicated, susceptible to hardware failures, and interrupted by bad weather, which limits the practical application of the smart rotor concept. On the other hand, with the increasing of wind turbine size (e.g. the aimed 20 MW wind turbine requires blades each with length over 120 meters), there are really no much choices to stabilise the blades. Thus some innovation design on smart rotor becomes crucial.

In this paper, we propose the use of passive mechanical network to drive the flaps as an alternative solution. The mechanical network consists of passive mechanical elements that do not require power supply or sensors. The mechanically driven flap mechanism guarantees the reliability and serviceability of the control system. Compared with other passive methods, mechanically driven flap is more robust and effective than stall control, aeroelastic tailoring and further lowers maintenance requirements. Here we give some brief background on mechanical network synthesis. A new two-terminal mechanical element named inerter was introduced by M.C. Smith [17] with the property that the force applied at the terminals is proportional to the relative acceleration between them. The inerter can thus replace the mass element to redefine the electrical-mechanical analogy so that the electrical circuit synthesis theory could be translated over to the mechanical networks. The mechanical network takes the form of an admittance function, which is defined to be the ratio of "through" variables to "across" variables in electrical circuit. We refer to Chen et al. [18], [19], [20], [21] and the references therein for the details on the synthesis of mechanical networks, which provided a guideline on realizing the mechanical network with least number of elements and restricted complexity to guarantee its reliability.

The modelling and control of long-span suspension bridges with mechanically driven flaps had been studied previously in [22], [23], [24], [25]. Zhao et al. [23], [24] designed the control system using pinion, rack and passive mechanical network, through which the trailing-edge flap is controlled. Bakis et al. [26] utilized passive rotational mechanical components to control leading and trailing-edge flaps. They both used the two-dimensional aeroelastic model of long-span suspension bridges for mechanical controller design and simulation. The critical flutter speed was increased

by around 35% and marked reductions on buffet responses were achieved fon long-span suspension bridges. Zhao et al. [24] also conducted wind tunnel experiments [27] to test the controller and substantial suppression on buffet response was achieved.

The success of implementing mechanical network on long-span suspension bridges can potentially be translated over to wind turbines because the cross-section of streamlined decks of suspension bridges bears resemblance to the aerofoil of wind turbine blades. Additionally, the application of the mechanical network thus far on aeroelastic systems had been on two-dimensional models where three-dimensional effects are not considered. Hence, in this paper, a mechanical network enabled aeroelastic model of the wind turbine is derived and used to demonstrate aeroelastic load reductions using trailing-edge flap that are passively controlled by the mechanical networks. We would like to mention that Hu [28, 29] made use of mechanical networks (including inerter) on the vibration reduction of wind turbine tower.

The structure of this paper is as follows: Section 2 describes the coupled model of structural dynamics and unsteady aerodynamics with the inclusion of flap dynamics, Section 3 presents the mechanical network synthesis and design process followed by the parametric optimisation of the mechanical network and flap configuration through H_∞ and H_2 schemes. Section 4 demonstrates the effectiveness of mechanical controller through simulation studies, which is followed by the conclusion in Section 5.

2. Methodology

The state-space aeroservoelastic formulation of the NREL 5MW wind turbine [30] with trailing-edge flap is presented in this section. It will first introduce the structural formulation, vortex-based unsteady aerodynamics and their coupling, followed by the derivation of the state-space representation that includes the flap dynamics for mechanical network synthesis.

2.1. Aeroservoelastic Model

The aeroservoelastic modeling of the wind turbine couples the multi-body composite beam structural description in a moving frame of reference (FoR) to the unsteady vortex-lattice method (UVLM) for the aerodynamics description [31, 32]. Three identical blades are azimuthally spaced at 120° apart from each other and connected to the shaft. The configuration of multi-body components of the wind turbine is shown in Fig. 1, comprising of three frames of reference, tower base FoR A, tower top FoR B_t and rotor hub FoR S. The blades and tower are modeled using beam elements and their structural dynamics are described with respect to hub frame S and tower base frame A [31]. The three-dimensional blades and tower are reduced

to one-dimensional representations through a cross-section analysis methodology. The velocities of frame S fixed to the rotor hub are constrained, using Lagrange multipliers, to match the nodal velocities of the local frame B_t at the tower top and the rotor angular speed [31, 33]. The equation-of-motion describing the structural dynamics of the wind turbine can be represented by

$$\boldsymbol{\mathcal{M}}(\ddot{\boldsymbol{\eta}}, \dot{\boldsymbol{\nu}}) + \boldsymbol{Q_{stif}}(\boldsymbol{\eta}) + \boldsymbol{Q_{gyr}}(\boldsymbol{\eta}, \dot{\boldsymbol{\eta}}, \boldsymbol{\nu}) + \boldsymbol{\Phi}(\boldsymbol{\lambda}, \dot{\boldsymbol{\lambda}}) = \boldsymbol{Q_{ext}}, \tag{1}$$

where $\boldsymbol{\eta}$ includes nodal displacements and rotations along the blade, shaft and tower. $\boldsymbol{\nu}$ represents the rigid-body velocities of the hub reference frame S and tower top frame B_t. $\boldsymbol{\mathcal{M}}$ is the discrete mass matrix. $\boldsymbol{Q_{ext}}$, $\boldsymbol{Q_{stif}}$ and $\boldsymbol{Q_{gyr}}$ represents the discrete external, elastic and gyroscopic forces. The rotor and tower is constrained by the matrix $\boldsymbol{\Phi}$ containing the Lagrange multiplier $\boldsymbol{\lambda}$ that constrains the velocities of rotor hub S to the tower top. The rotational speed of the rotor can be prescribed through $\boldsymbol{\lambda}$.

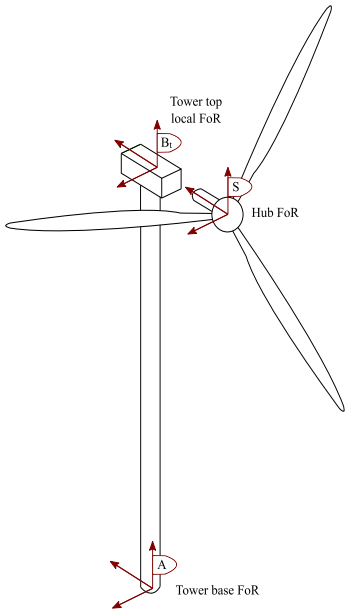

Figure 1: Multi-body configuration of the wind turbine.

The unsteady aerodynamics of the wind turbine is modeled using the discrete-time unsteady vortex-lattice method (UVLM) with a prescribed helicoidal wake, thus ignoring wake roll-up so as to enable a linear presentation [34, 35, 36]. In the UVLM, vortex rings are used as fundamental solutions to represent the lifting surface (blade) and the wake. The non-penetrating (Neumann) boundary condition is imposed for

three blades neglecting the aerodynamic interference with hub and tower such that

$$\sum_{i=1}^{N}\left(\sum_{j=1}^{N}\left(\mathbf{A}_{b,ij}\mathbf{\Gamma}_{b,j}+\mathbf{A}_{w,ij}\mathbf{\Gamma}_{w,j}\right)+\boldsymbol{w_i}\right)=\mathbf{0}, \tag{2}$$

where $\mathbf{\Gamma}_{b,j}$ and $\mathbf{\Gamma}_{w,j}$ denote the circulation strengths of the bound and wake vortex rings, respectively, and N is the number of blades. The aerodynamic influence coefficients $\mathbf{A}_{b,ij}$ and $\mathbf{A}_{w,ij}$, are obtained from the Biot-Savart law to account for the velocity induced normal to the lifting surface by the blades and wake, respectively. Equation (2) states that the normal velocity at each collocation point caused by vortices and motion of blade and flap has to be zero. The downwash acting on the blade due to motion of the lifting surface and control surface is represented by $\boldsymbol{w}_i$. The aerodynamic forces and moments are computed from the pressure distributions across panels on the blades through the unsteady Bernoulli equation which in compact form can be written as $\Delta P_k^{n+1} = \Phi\mathbf{\Gamma}_b^{n+1} + \Phi_k^n\mathbf{\Gamma}_b^n$ where Φ_k is a row vector containing the coefficients of the unsteady Bernoulli equation [32] and $\mathbf{\Gamma_b}$ contains circulation strengths of all vortex rings on the blades.

These aerodynamic forces and moments are then coupled to the discretized structural dynamics by mapping them to the corresponding structural nodes, and in turn, mapping the structural displacements and velocities of each node to their respective collocation points as downwash.

2.2. Inclusion of Flap Dynamics

To incorporate flap dynamics into the blades, the structural dynamics in (1) is modified. The schematic representation for one of the three identical blades is shown in Fig. 2 with flap mean position, flap span, and flap chord given by [31]. The properties of the blade in [30] are adopted as the benchmark for the characteristic definition of the blade in Fig. 2. The blade length along the preconed axis is 60 m (ignoring the root of circular cross section) and the overall mass is 17740 kg. More detailed properties used in this paper is listed in Table 1. The left slash area represents the hub on which the blades are fixed. In this study, the flap span, flap chord and flap mean position are optimised in Section 3 to reach a optimal configuration for blade load alleviation in the closed loop system. Along each discrete chordwise section of the lifting surface containing the trailing-edge flap, the dynamics of the flap can be described using the sectional model as given in Fig. 3. The distance between the elastic axis (EA) and the trailing-edge of blade is represented by $2bp$ in Fig. 3. As the elastic axis of the blade is aft 25% chord from the leading edge, hence $p = 1 - 0.25 = 0.75$.

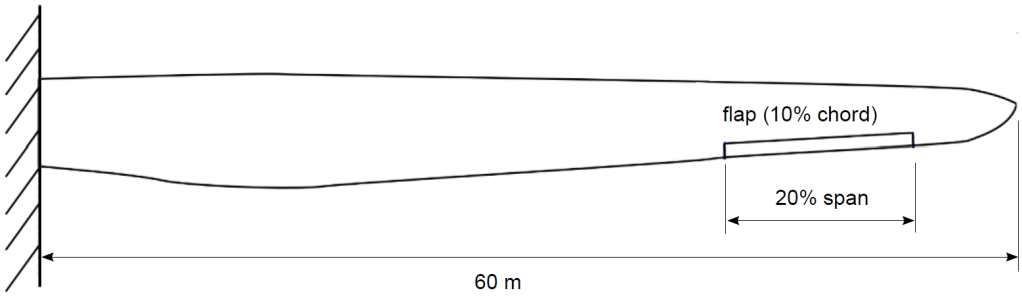

Figure 2: Configuration of flap on the wind turbine blade. Flap occupies 20% span, 10% local chord and is located at a mean position of 80% span.

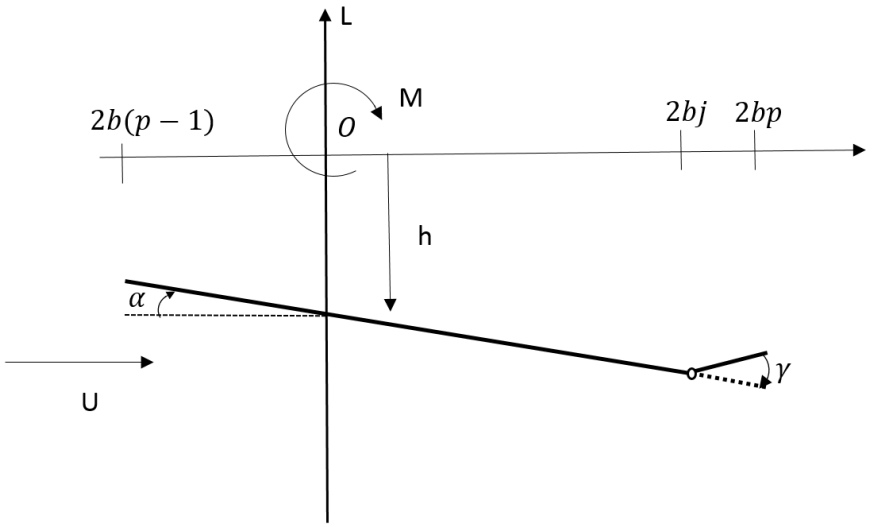

Figure 3: Cross-section of blade containing the trailing-edge flap. The wind speed is represented by U, plunge by h, lifting force by L and elastic axis by EA. The moment M, pitch angle α and flap angle γ are positive clockwise. b is the half chord length and the flap chord is $2b(j-q)$. Parameters j and p represent the leading edge and trailing-edge of the flap, respectively.

The dynamic equation-of-motion for an aerofoil section is

$$\boldsymbol{\mathcal{M}}_a\ddot{\boldsymbol{q}} + \boldsymbol{\mathcal{C}}_a\dot{\boldsymbol{q}} + \boldsymbol{\mathcal{K}}_a\boldsymbol{q} = \boldsymbol{Q} \tag{3}$$

where $\boldsymbol{\mathcal{M}}_a = \begin{bmatrix} m & S_\alpha & S_\gamma \\ S_\alpha & I_\alpha & (I_\gamma + 2bjS_\gamma) \\ S_\gamma & (I_\gamma + 2bjS_\gamma) & I_\gamma \end{bmatrix}$, $\boldsymbol{q} = \begin{bmatrix} \ddot{h} \\ \ddot{\alpha} \\ \ddot{\gamma} \end{bmatrix}$, $\boldsymbol{\mathcal{C}}_a = \begin{bmatrix} C_h & 0 & 0 \\ 0 & C_\alpha & 0 \\ 0 & 0 & C_\gamma \end{bmatrix}$, $\boldsymbol{\mathcal{K}}_a = \begin{bmatrix} K_h & 0 & 0 \\ 0 & K_\alpha & 0 \\ 0 & 0 & K_\gamma \end{bmatrix}$ and $\boldsymbol{Q} = \begin{bmatrix} L \\ M^\alpha \\ M^\gamma + M^c \end{bmatrix}$. The quantity m in above equation is the mass per unit span of the blade and flap combination. S_α and S_γ are the first moments of area computed by integration over the blade and trailing-edge flap domains A_b, A_t, given by

$$\begin{aligned} S_\alpha &= \int_{A_b+A_t} r dm \\ S_\gamma &= \int_{A_t} (r - 2bj) dm. \end{aligned} \tag{4}$$

Quantities m_b and m_γ are the masses of blade and flap per unit length, respectively (note : $m = m_b + m_\gamma$). L and M^α are the aerodynamic lift and aerodynamic moment acting about the elastic axis (EA) while M^γ and M^c are the aerodynamic moment and control torque about the flap hinge. I_α and I_γ are the second order moments of inertia per-unit-length, given by

$$\begin{aligned} I_\alpha &= \int_{A_b+A_t} r^2 dm, \\ I_\gamma &= \int_{A_t} (r - 2bj)^2 dm. \end{aligned} \tag{5}$$

K_h and K_α are the bending and torsional stiffnesses of the wind turbine blade, respectively. The flap spring stiffness is calculated using $K_\gamma = I_\gamma \omega_\gamma^2$, where ω_γ is the resonant frequency of flap. C_h and C_α are the corresponding bending and torsional damping terms of the wind turbine blade, respectively. The flap damping coefficient is obtained by $C_\gamma = 2\zeta_\gamma I_\gamma \omega_\gamma$, where ζ_γ is the damping ratio. As the flap occupies 10% chord, The parameter $j = p - 0.1 = 0.75 - 0.1 = 0.65$.

Along the sections of the blade containing the flaps, the structural equation-of-

Table 1: Physical parameters of NREL 5MW wind turbine blade with controllable trailing-edge flap

Parameters	Symbol	Values
Half chord	b	1.365 m
Leading edge coefficient of the flap	j	0.65
Trailing edge coefficient of the flap	p	0.75
Blade mass per unit length	m_b	102.5 kg
Torsional stiffness of the blade	K_α	1.256×10^7 Nm/rad
Bending stiffness of the blade	K_h	7.098×10^7 N/m
Torsional damping coefficient of the blade	C_α	799.47 Nm·s/rad
Bending damping coefficient of the blade	C_h	460.25 N·s/m
Resonant frequency of the flap	ω_γ	58 rad/s
Damping ratio of the flap	ζ_γ	0.02
Flap mass per unit length	m_γ	11.39 kg/m

motion in (1) is first linearised around a constant rotor angular velocity and augmented with an additional degree of freedom γ, the flap deflection angle, to incorporate the flap dynamics. The resulting equations-of-motion of the wind turbine is given by

$$\begin{bmatrix} \boldsymbol{\mathcal{M}}_t^{SS} & \mathbf{0} & \mathbf{0} & \mathbf{0} & -\boldsymbol{\Lambda}^T \\ \mathbf{0} & \boldsymbol{\mathcal{M}}_r^{SS} & \boldsymbol{\mathcal{M}}_r^{SR} & \boldsymbol{\mathcal{M}}_\gamma^T & \mathbf{0} \\ \mathbf{0} & \boldsymbol{\mathcal{M}}_r^{RS} & \boldsymbol{\mathcal{M}}_r^{RR} & \mathbf{0} & \boldsymbol{A}_{cc}^T(\theta) \\ \mathbf{0} & \boldsymbol{\mathcal{M}}_\gamma & \mathbf{0} & \boldsymbol{I}_\gamma & \mathbf{0} \\ \mathbf{0} & \mathbf{0} & \mathbf{0} & \mathbf{0} & \mathbf{0} \end{bmatrix} \begin{Bmatrix} \Delta\ddot{\boldsymbol{\eta}}_t \\ \Delta\ddot{\boldsymbol{\eta}}_r \\ \Delta\dot{\boldsymbol{\nu}}_r \\ \Delta\ddot{\boldsymbol{\gamma}} \\ \Delta\dot{\boldsymbol{\lambda}} \end{Bmatrix} + \begin{bmatrix} \boldsymbol{\mathcal{C}}_t^{SS} & \mathbf{0} & \mathbf{0} & \mathbf{0} & \mathbf{0} \\ \mathbf{0} & \boldsymbol{\mathcal{C}}_r^{SS} & \boldsymbol{\mathcal{C}}_r^{SR} & \mathbf{0} & \mathbf{0} \\ \mathbf{0} & \boldsymbol{\mathcal{C}}_r^{RS} & \boldsymbol{\mathcal{C}}_r^{RR} & \mathbf{0} & \mathbf{0} \\ \mathbf{0} & \mathbf{0} & \mathbf{0} & \boldsymbol{\mathcal{C}}_\gamma & \mathbf{0} \\ \boldsymbol{\Lambda} & \mathbf{0} & -\boldsymbol{A}_{cc}(\theta) & \mathbf{0} & \mathbf{0} \end{bmatrix} \begin{Bmatrix} \Delta\dot{\boldsymbol{\eta}}_t \\ \Delta\dot{\boldsymbol{\eta}}_r \\ \Delta\boldsymbol{\nu}_r \\ \Delta\dot{\boldsymbol{\gamma}} \\ \Delta\boldsymbol{\lambda} \end{Bmatrix} + \begin{bmatrix} \boldsymbol{\mathcal{K}}_t^{SS} & \mathbf{0} & \mathbf{0} & \mathbf{0} & \mathbf{0} \\ \mathbf{0} & \boldsymbol{\mathcal{K}}_r^{SS} & \mathbf{0} & \mathbf{0} & \mathbf{0} \\ \mathbf{0} & \boldsymbol{\mathcal{K}}_r^{RS} & \mathbf{0} & \mathbf{0} & \mathbf{0} \\ \mathbf{0} & \mathbf{0} & \mathbf{0} & \boldsymbol{\mathcal{K}}_\gamma & \mathbf{0} \\ \mathbf{0} & \mathbf{0} & \mathbf{0} & \mathbf{0} & \mathbf{0} \end{bmatrix} \begin{Bmatrix} \Delta\boldsymbol{\eta}_t \\ \Delta\boldsymbol{\eta}_r \\ \mathbf{0} \\ \boldsymbol{\gamma} \\ \mathbf{0} \end{Bmatrix} = \begin{Bmatrix} \mathbf{0} \\ \boldsymbol{Q}_{ext} \\ \int \boldsymbol{Q}_{ext} \\ \boldsymbol{M}^\gamma + \boldsymbol{M}^c \\ \mathbf{0} \end{Bmatrix}, \tag{6}$$

where the subscripts t and r represent the tower and rotor, while the superscripts R and S represent the rigid-body and structural contributions, respectively. The matrices $\boldsymbol{A}_{cc}(\theta)$ and $\boldsymbol{\Lambda}$ enforce the velocity constraints between the tower top and rotor hub with prescribed azimuth angle of the rotor blades $\theta = \Omega t$ where Ω is the rotor angular velocity. The overall forces and moments on rotor hub $\int \boldsymbol{Q}_{ext}$ balances forces due to motion of the tower. Flap dynamics appear in the fourth row and have

the same meaning as in the aerofoil configuration in (3) with $\boldsymbol{M}_\gamma$ and $\boldsymbol{I}_\gamma$ accounting for the flap dynamics. As before, $\boldsymbol{M}^\gamma$ and $\boldsymbol{M}^c$ are the aerodynamic moment and control torque about the flap hinge, but in bold to represent concatenated matrices for the three blades.

The structural equation of motions given in (6) are discretized using the Newmark-β method and coupled with the discrete-time UVLM in (2). To resolve the aerodynamic forces acting on the wind turbine blade as well as the aerodynamic moment about flap hinge $\boldsymbol{M}^\gamma$, the unsteady Bernoulli equation is used. We adopt 20 and 19 panels in spanwise and chordwise direction in the modelling, respectively, which result in the state matrix A with 5925 states and input matrix B with 63 inputs. The assembled state-space aeroservoelastic representation of the wind turbine blades is represented by

$$\begin{aligned} \boldsymbol{x}^{n+1} &= \boldsymbol{A}(\theta)\boldsymbol{x}^n + \boldsymbol{B}\boldsymbol{u}^n + \boldsymbol{G}\boldsymbol{w}^n, \\ \boldsymbol{y}^n &= \boldsymbol{C}\boldsymbol{x}^n + \boldsymbol{D}\boldsymbol{u}^n + \boldsymbol{H}\boldsymbol{w}^n, \end{aligned} \tag{7}$$

where $\mathbf{x}^T = \left[\Delta\boldsymbol{\Gamma}^T | \Delta\boldsymbol{\eta}_t^\top \Delta\dot{\boldsymbol{\eta}}_t^\top \Delta\boldsymbol{\eta}_r^\top \Delta\dot{\boldsymbol{\eta}}_r^\top | \Delta\boldsymbol{\nu}^\top | \Delta\boldsymbol{\gamma}^\top \Delta\dot{\boldsymbol{\gamma}}^\top | \Delta\boldsymbol{\lambda}^\top\right]$ contains the aerodynamic states for all three blades and wake, structural states, rigid-body states, flap states and the constraints. The state matrix $\boldsymbol{A}$ is a function of the rotor azimuth angle, which defines the rotor orientation with respect to the tower at each time-step. This results in a system that is linear parameter-varying, as θ is a function of the time-step. The inputs $\boldsymbol{u}$ and $\boldsymbol{w}$ in (7) are the flap control torque $\boldsymbol{M^c}$ and external disturbances, respectively. There are 17 output variables in total. The first three are the blade root-torsional moment (RTM) for every blade and the following three outputs are the RBM for each blade. The next two outputs are the side-side and fore-aft motions of the tower top. The tip deflection of the three blades are the following outputs. The rest are the flap angles and angular velocities for the trailing-edge flaps mounted on the three blades.

The aeroelastic description derived above is used to model the NREL 5-MW reference wind turbine [30] in this paper. Two-node beam elements are used to model the tower and rotor blades, which are also connected by Lagrange multipliers. The nacelle and hub are modelled as point masses on the tower top at prescribed offset locations [31]. For the aerodynamic model, the vortex panels are distributed in the outer 80% span of the turbine blade and the helicoidal wake profile is prescribed with the inflow and rotational velocity [31].

The turbulence is generated by TurbSim, an open-source stochastic inflow turbulence tool, developed by National Renewable Energy Laboratory in the US, see Section 4 for details.

3. Mechanical Controller Design

The mechanical network synthesis theory is first introduced, followed by the closed-loop control system of the aeroservoelastic system. Lastly, the procedure for parametric optimisation of the mechanical controller is presented.

3.1. Mechanical Network Synthesis Theory

The mechanical controller of flap on each wind turbine blade is designed based on the aeroelastic system of a single rotating blade without the influence of the tower. Without tower dynamics, the state matrix for the rotor, and hence each blade, becomes linear as the azimuth dependence of tower top motion on the blade root is removed. In the description of a single blade, the aerodynamics in (3) will have $N = 1$. For the structural dynamics in (6), all terms with superscript R corresponding to rigid-body motion will be neglected, including the rigid-body states and constraints. This results in a linear coupled system given by

$$\begin{aligned} \boldsymbol{x_s}^{n+1} &= \boldsymbol{A}_s \boldsymbol{x}_s^n + \boldsymbol{B}_s u_s^n + \boldsymbol{G}_s \boldsymbol{w}_s^n, \\ \boldsymbol{y}_s^n &= \boldsymbol{C}_s \boldsymbol{x}_s^n + \boldsymbol{D}_s u_s^n + \boldsymbol{H}_s \boldsymbol{w}_s^n, \end{aligned} \tag{8}$$

where the subscript s denotes a single blade and the state vector contains only the aerodynamic and structural states for a single rotating blade with gyroscopic contribution to the damping and stiffness matrices. With the same number of spanwise and chordwise panels used in (7), the state matrix and input matrix in (8) contain 1617 states and 21 inputs.

The inclusion of flap deflection and its rates as state variables in (7) and (8) enables the utilization of mechanical network as the controller. The control input to the system would be the torque (called "through" variable) generated by mechanical network while the flap angular velocity (called "across" variable) is the input to the mechanical network. The parameters of admittance function are optimised by H_∞ and H_2 optimization schemes with constraints alongside, which ensure the stability of closed-loop system and can be synthesised by springs, dampers and inerters.

3.2. Feedback System

The block diagram of the closed-loop control system is shown in Fig. 4. Plant P represents the open-loop fluid-structural coupled system demonstrated in (8) while $\boldsymbol{w}_s$ represents the wind disturbances and $\boldsymbol{y}_s$ are the outputs. K denotes the mechanical network with flap angular velocity $\dot{\gamma}$ as input and flap control torque M^c as output.

Fig. 5 shows the sketch of the practical implementation of the passive blade-flap configuration system. The mechanical network is connected between the blade and

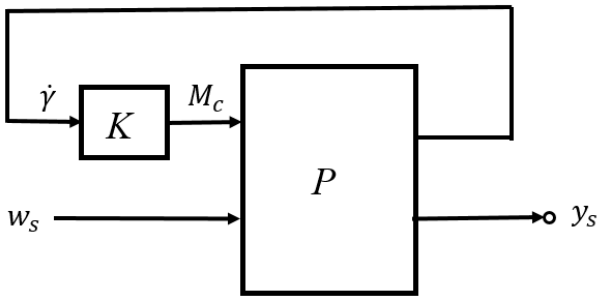

Figure 4: Block diagram of the closed-loop feedback system.

flap hinge. It consists of springs, dampers and inerters with their admittance functions defined as k/s, c and ds, respectively. Parameters k, c, d and s are the spring stiffness, damping coefficient, inertance and Laplace transform variable, respectively. The admittance function of series and parallel connection of these passive components is an analogy to the admittance function of corresponding connection of capacitors in electrical circuit. The resulting mechanical network admittance function will be in the form of a transfer function in continuous time domain after combining these components. In the optimisation and simulation process, we discretize the admittance function of the mechanical network to be consistent with the plant in discrete time.

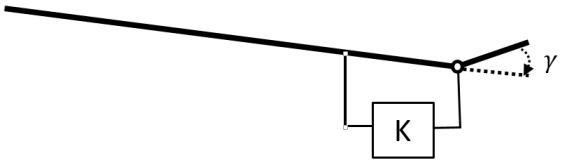

Figure 5: Sketch of the practical implementation of the passive blade-flap configuration system. K is the mechanical network attached between the blade and the hinge of the trailing-edge flap.

3.3. Optimisation of the Controller

The parameters of the admittance function of mechanical network are optimised by two optimisation schemes. The admittance function of mechanical network in discrete-time domain is represented by K. The first optimization scheme minimizes the H_∞ norm of sensitivity $S = (I + PK)^{-1}$. The second scheme minimizes the H_2 norm of the transfer function T, which maps wind disturbances to flapwise RBM and tip deflection.

We design two structures for the mechanical network controller as shown in Fig. 6. Their admittance functions are $Y_1(s) = \dfrac{ds(c+\frac{k}{s})}{ds+(c+\frac{k}{s})} = \dfrac{dcs^2+dks}{ds^2+sc+k}$ and $Y_2(s) = \dfrac{c_1(ds+c_2+\frac{k}{s})}{c_1+(ds+c_2+\frac{k}{s})} = \dfrac{dc_1s^2+c_1c_2s+c_1k}{ds^2+(c_1+c_2)s+k}$ with the parameters d, c, $c1$, $c2$ and k to be optimised. The spring, damper and inerter used in Fig. 6 are in the rotational form, which means that they are in moment-angular velocity form. We consider two cases: the first one is to optimise the parameters of the mechanical network while the second one is to optimise the parameters of the mechanical network and the flaps. The flap has three parameters to optimise, where fm, fs and fc represent the mean position of the flap, the spanwise length and chordwise length of the flap, respectively. The optimisation method used is MATLAB sequential quadratic programming algorithm FMINCON. Four constraints are added alongside the optimisation process. The first one constrains all the eigenvalues of the closed-loop system to lie in the unit circle to ensure stability. The second one requires the parameters of admittance functions $Y_1(s)$ and $Y_2(s)$ to be non-negative so that the mechanical network could be synthesised. The third one constraints the length of flap less than 30% of the length of blade in spanwise direction as well as the distance between the blade tip position and flap tip position greater than 5% length of the blade in spanwise direction. The fourth one requires that the flap occupies less than 15% of the blade in chordwise direction.

For the H_∞ optimisation scheme, the H_∞ norm of the sensitivity S, denoted as $\|S\|_\infty$, is related to the robustness against additive perturbation on the loop transfer function PK [26]. The optimisation objective is given by

$$\min_e \|S(e)\|_\infty, \tag{9}$$

where e is the parameter set of the mechanical network. The smaller the value of $\|S(e)\|_\infty$, the more robust the system is in rejecting disturbances and uncertainties.

For the H_2 optimisation scheme, the H_2 norm of T is minimized for minimum flapwise RBM and tip deflection with all the other conditions remaining the same as the previous case. The objective function is given by

$$\min_e \|T(e)\|_2, \tag{10}$$

where $\|\cdot\|_2$ denotes the H_2 norm and $T(e)$ represents the closed-loop transfer function that maps disturbances to flapwise RBM and tip deflection. The smaller the value

of $\|T(e)\|_2$, the smaller the flapwise RBM and tip deflection response.

3.3.1. Optimization results with given flap configuration parameters

The flap configuration parameters given in [31] mounts the flap at a mean position of 80% span from blade root and occupies 20% span and 10% chord. Utilizing these flap configuration parameters, mechanical networks K1 and K2 are developed with H_∞ and H_2 optimisation schemes, respectively. K1 and K2 are separately set equal to the admittance functions $Y_1(s)$ and $Y_2(s)$ for optimisation. The optimisation results for K1 is to take the form of admittance function $Y_1(s)$, where $c = 43.2$ Nm $\cdot$ s/rad, $k = 89.4$ Nm/rad and $d = 12.4$ Nm $\cdot$ s^2/rad. On the other hand, the optimisation results for K2 with H_2 optimization scheme is to take the form of admittance function $Y_1(s)$ as well, where $c = 97.1$ Nm $\cdot$ s/rad, $k = 120.76$ Nm/rad and $d = 7.25$ Nm $\cdot$ s^2/rad.

3.3.2. Optimization results with optimised flap configuration parameters

Including the flap configuration parameters into the optimisation process, we obtained the results for the two optimisation schemes that correspond to mechanical networks K3 and K4, respectively. K3 and K4 are separately set equal to the admittance functions $Y_1(s)$ and $Y_2(s)$ for their optimisation process. For the H_∞ optimization scheme, the optimisation results for flap configuration parameters are $fm = 0.805$, $fs = 0.286$ and $fc = 0.127$. It means that the flap is mounted on the blade trailing-edge with its mean position at 80.5% of the blade. The spanwise and chordwise length of flap occupy 28.6% span and 12.7% chord of blade respectively. The results for mechanical network K3 is to take the form of admittance function $Y_2(s)$, where $c_1 = 27.74$ Nm $\cdot$ s/rad, $c_2 = 52.14$ Nm $\cdot$ s/rad, $k = 172.3$ Nm/rad and $d = 6.26$ Nm $\cdot$ s^2/rad.

The optimisation results of flap configuration parameters for H_2 optimisation scheme are $fm = 0.812$, $fs = 0.262$ and $fc = 0.126$. The flap span in both cases are increased compared to that in [13]. This makes sense as a larger flap causes greater effect on local aerodynamics. The optimisation results for mechanical network K4 is to take the form of admittance function $Y_1(s)$, where $c = 32.3$ Nm $\cdot$ s/rad, $k = 64.7$ Nm/rad and $d = 12.3$ Nm $\cdot$ s^2/rad.

The passive components shown in Fig. 6 are all in rotational form to be installed on trailing-edge flap. It can be seen that the structure of the two mechanical networks are very simple with 4 passive elements at most, hence its reliability is ensured.

4. SIMULATION RESULTS

The mechanical controllers, K1 and K2, obtained above are both optimised with the flap configuration parameters given in [31] through H_∞ and H_2 optimisation

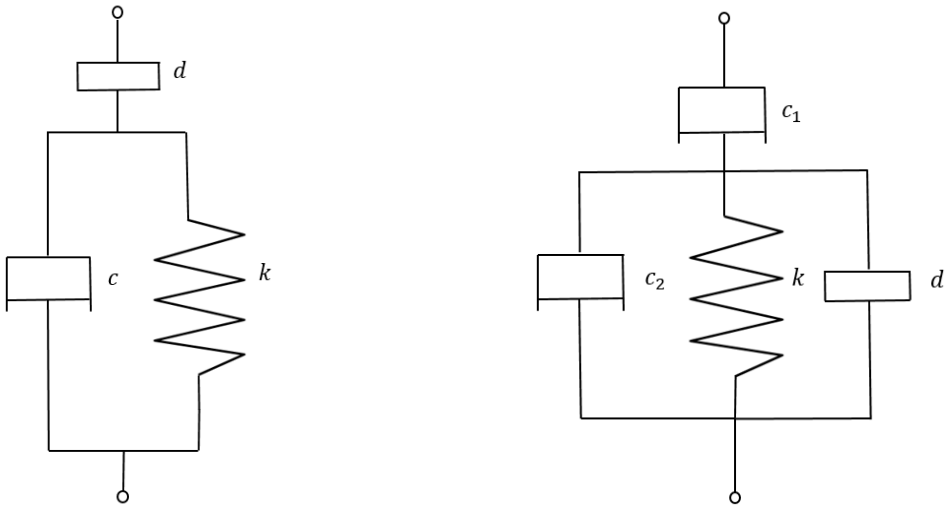

(a) $Y_1(s)$ (b) $Y_2(s)$

Figure 6: Schematic realisation of two mechanical networks $Y_1(s)$ and $Y_2(s)$

schemes, respectively. Mechanical networks K3 and K4 are optimised together with the flap configuration parameters fm, fs, fc through H_∞ and H_2 optimization schemes, respectively. As mentioned in Section 2, we generate turbulence through TurbSim. In the setup of the Turbsim input file, the International Electrotechnical Commission (IEC) standard was chosen to be 61400-1 [37] and von Karman spectral model was used. Moreover, we set the IEC turbulence model to be Normal Turbulence Model (NTM), Extreme Turbulence Model (ETM) and Extreme Wind Speed Model (EWM), which correspond to the design load cases (DLCs) 1.2, 1.3 and 6.1, to test three types of load profiles. The mean wind speed is 14 m/s with turbulence intensity of 17.5%. The generated wind filed is in the grid size of 31 $\times$ 31. Apart from the turbulence, we also conduct the simulation using harmonic gust with a mathematical representation of $0.1 \times sin(\omega t)$. The frequency of the harmonic gust varies from 0.3 rad/s to 1 rad/s with a step of 0.1 rad/s. Several key indexes are compared to demonstrate the performances of controllers, which include the flapwise RBM, blade RTM, blade tip deflection (BTD), tower top fore-aft deflection (TTFAD) and flap angle. The performances of K1, K2, K3 and K4 on mitigating fatigue loads (DLC 1.2), blade tip deflection, tower vibrations and harmonic gust load are summarized in Table 2. For the indexes such as RBM, RTM and TTFAD, we examine the root mean square (RMS) reduction while, for the BTD and flap angle, we examine the maximum absolute value reduction. The RMS reduction and maximum value

reduction given in Table 2 were obtained by calculating the increase or decrease percentage of corresponding values of each index for the case with controller relative to the case without flap.

Table 2: Closed-loop alleviation of blade loads under the case of DLC 1.2 and gust excitations with flaps actuated by controllers K1, K2, K3 and K4. Negative sign implies an increase. The abbreviations are: rms (root-mean-square), RBM (root-bending moment), RTM (root-torsion moment) BTD (balde tip deflection), rd (reduction), GT (gust), TTFAD (tower top fore-aft deflection)

Controller name	%rd RMS RBM	%rd max BTD	max γ (°)	%rd RMS RTM	%rd RMS TTFAD
K1(DLC1.2)	11.49	10.82	9.73	-42.75	8.24
K2(DLC1.2)	12.64	12.42	10.57	-52.47	11.35
K3(DLC1.2)	15.13	15.83	13.96	-68.52	14.27
K4(DLC1.2)	16.76	18.27	14.31	-73.24	16.28
K1(GT)	9.38	11.42	10.73	-57.21	10.62
K2(GT)	11.64	14.67	11.28	-62.82	11.43
K3(GT)	14.27	16.38	13.71	-71.32	15.76
K4(GT)	16.73	18.45	14.26	-84.23	17.27

The simulation results of K1 in the case of DLC 1.2 are shown in Fig. 7 and Fig. 8. Fig. 7 demonstrates the time simulations of flapwise RBM, blade RTM and flap angle as a comparison with the wind turbine blades without flap, in which the curves for flapwise RBM and blade RTM are averaged across three blades. The blade tip deflection and tower top fore-aft deflection of K1 are presented in Fig. 8. The X coordinates of Fig. 7 and Fig. 8 are converted from time step to the number of rotation cycles according to the angular speed of the wind turbine, which provides clearer observation. Similar simulation results in the case of DLC 1.2 are presented for K2, K3 and K4 from Fig. 9 to Fig. 14 for clear observation.

It is observed from Table 2 that controller K2 outperforms controller K1 while controller K4 outperforms K3 with evident alleviation of flapwise RBM, blade tip deflection and tower top fore-aft deflection. This is due to the difference in optimisation objectives between the controllers. K1 and K3 are optimised with the priority to be robust against model uncertainties while K2 ad K4 are optimised to minimise the response of flapwise RBM and blade tip deflection. Besides, K3 achieves better load reduction performances than K1 and the same result applies to K4 and K2. This is due to the fact that the optimal flap position, flap span and flap chord are used for

K3 and K4 in simulation. The blade RTM is increased for all the controllers due to the additional moment imposed by flap deflection at the trailing-edge of the blade, which also occurs in the case of active controllers [13]. The maximum flap angle of all the controllers are kept small to be within the attached flow assumption of the modelling.

Comparing with the performance on load reduction of wind turbine blades by actively controlled flaps as in [13], the reduction on flapwise RBM by mechanical network K1 and K2 in Table 2 is slightly inferior, but they offer better reliability as power supply, sensor, and computer are not required. In average, the 13% RMS reduction on flapwise RBM, 11.1% RMS reduction on tower top deflection, 16% reduction on maximum blade tip deflection and 97.9% RMS increase on blade RTM were obtained by the H_∞ controller measuring the flapwise RBM as feedback in the similar flow conditions as in [13]. However, implementing the mechanical networks restrains the increase in blade RTM, as can be seen from Table 2 that the average increase on blade RTM is around 64.07%. Considering the augmentation of flap span, chord and the change of the mean position of the flap, we designed K3 and K4 with optimal flap configuration parameters. It can be observed from Table 2 that K3 and K4 achieved an average reduction of 15.72% on the flapwise RBM, 17.34% on blade tip deflection and 15.89% on tower top fore-aft deflection, which are better than the active controller in [13]. Besides, the increase on blade RTM is around 74.33% for K3 and K4, which is less than that of the active controller mentioned above. We set constraints on the flap configuration parameters in the process of optimisation to ensure the physical feasibility.

It is also interesting to examine the performances of the mechanical controllers in the case of ultimate loads. Thus, we conduct the simulations in the case of DLCs 1.3 and 6.1. It can be observed that the blade loads are reduced dramatically. The simulation results of the controller K4 are presented from Fig. 15 to Fig. 18 while other controllers have the similar trends, thus omitted but their performances are demonstrated in Table 3.

We mention that we tried to optimise a general second-order admittance function for mechanical networks, but found that the improvement was marginal compared to the mechanical networks presented above.

5. CONCLUSIONS

A three-dimensional aeroelastic system of wind turbine was presented coupling composite beam model description for the structural dynamics with the unsteady vortex-lattice method for the unsteady aerodynamics. A novel mechanical controller has

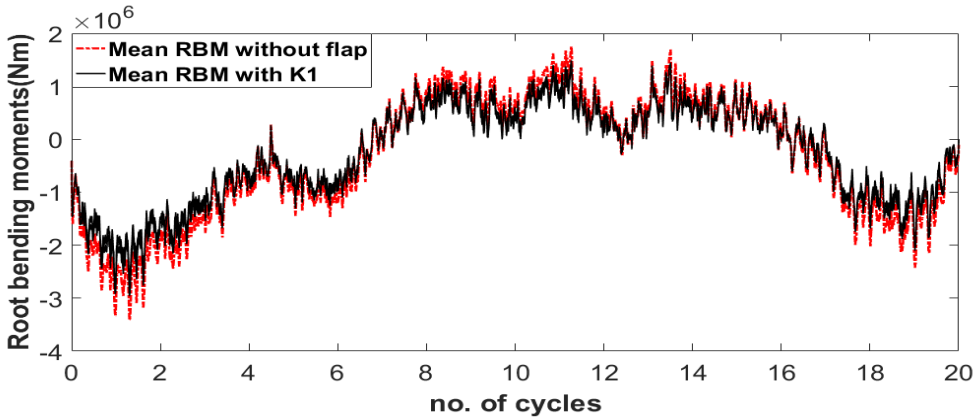

(a) Blade flapwaise RBM

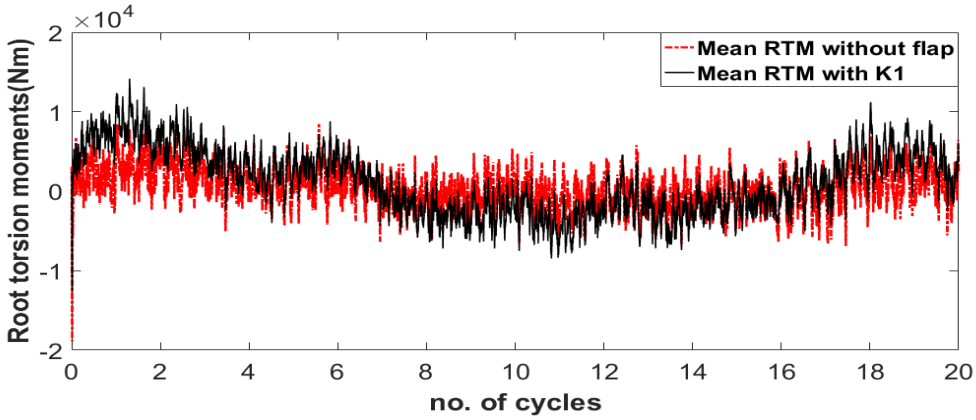

(b) Blade RTM

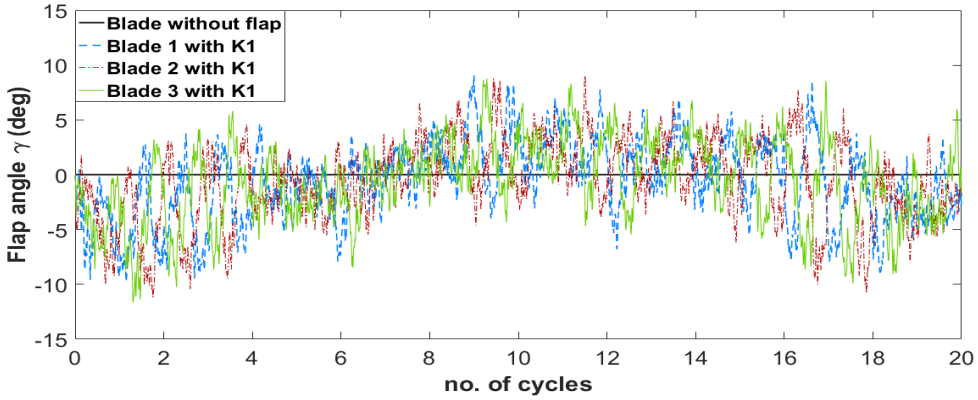

(c) Flap deflection angle

Figure 7: Time simulation for flapwise RBM, blade RTM and flap angle of wind turbine blades without and with flap actuated by controller K1, in a flow velocity of 14 m/s and turbulence intensity of 17.5%.

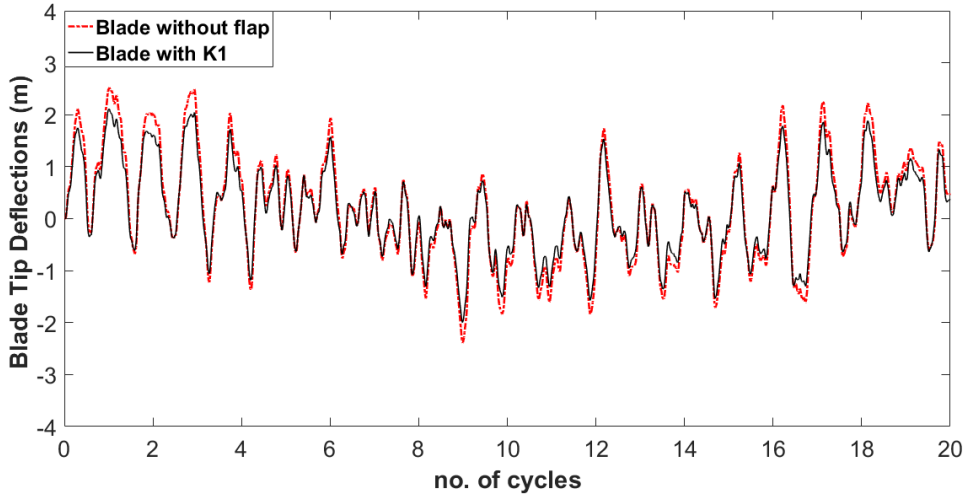

(a) Blade tip deflection

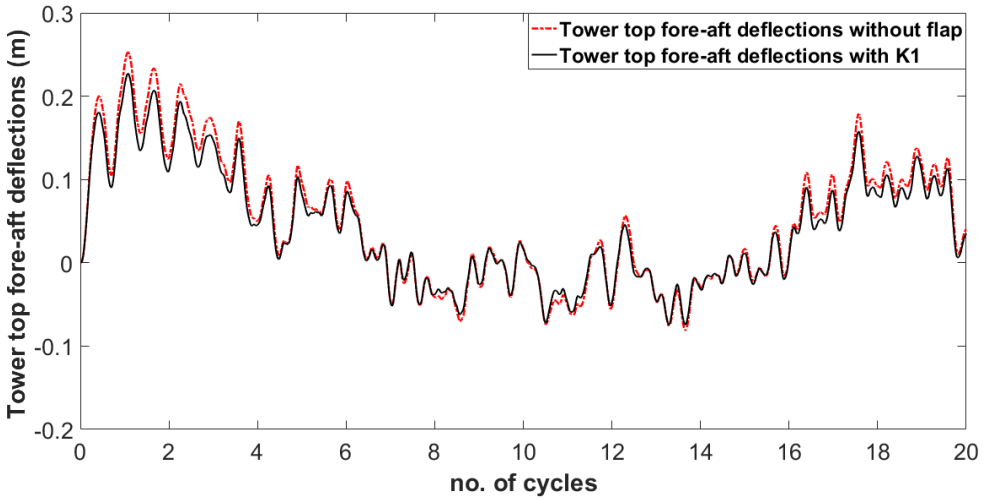

(b) Tower top fore-aft deflection

Figure 8: Time simulation for blade tip deflection and tower top fore-aft deflection of the wind turbine without and with flap actuated by controller K1, in a flow velocity of 14 m/s and turbulence intensity of 17.5%.

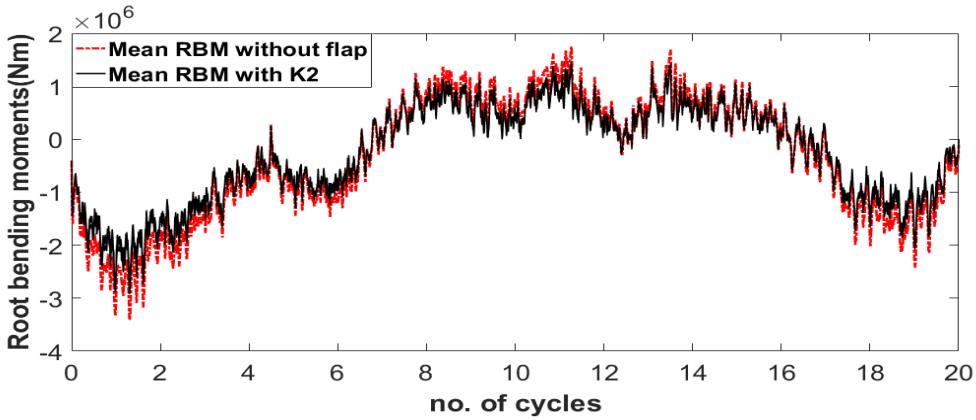

(a) Blade flapwaise RBM

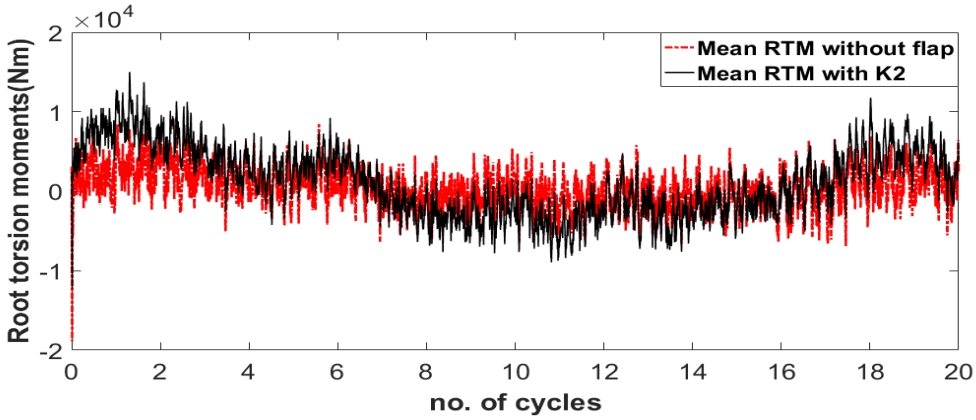

(b) Blade RTM

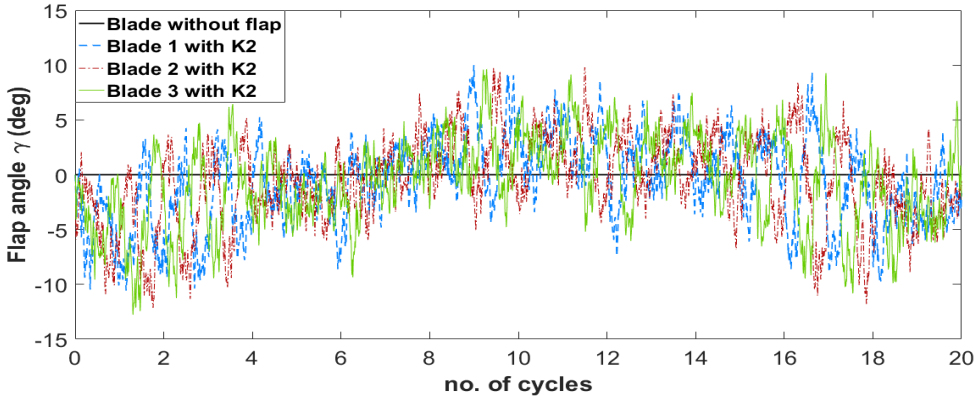

(c) Flap deflection angle

Figure 9: Time simulation for flapwise RBM, blade RTM and flap angle of wind turbine blades without and with flap actuated by controller K2, in a flow velocity of 14 m/s and turbulence intensity of 17.5%.

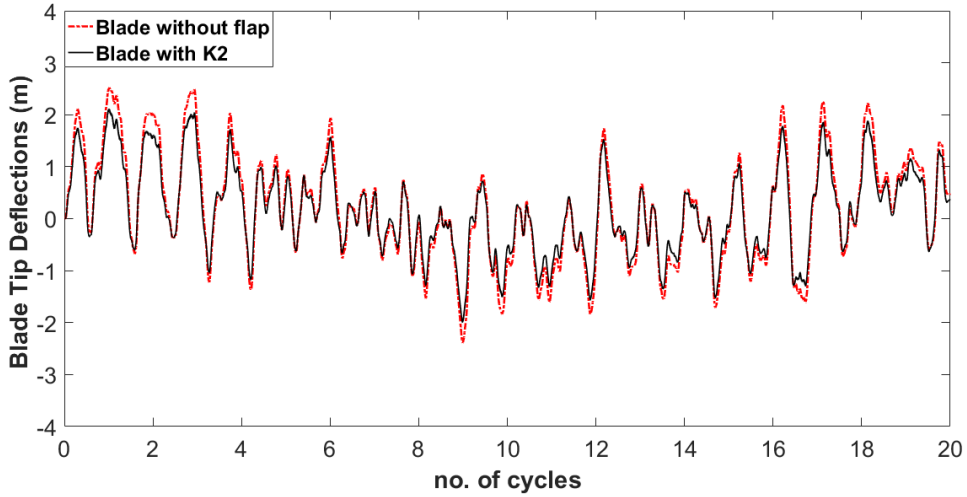

(a) Blade tip deflection

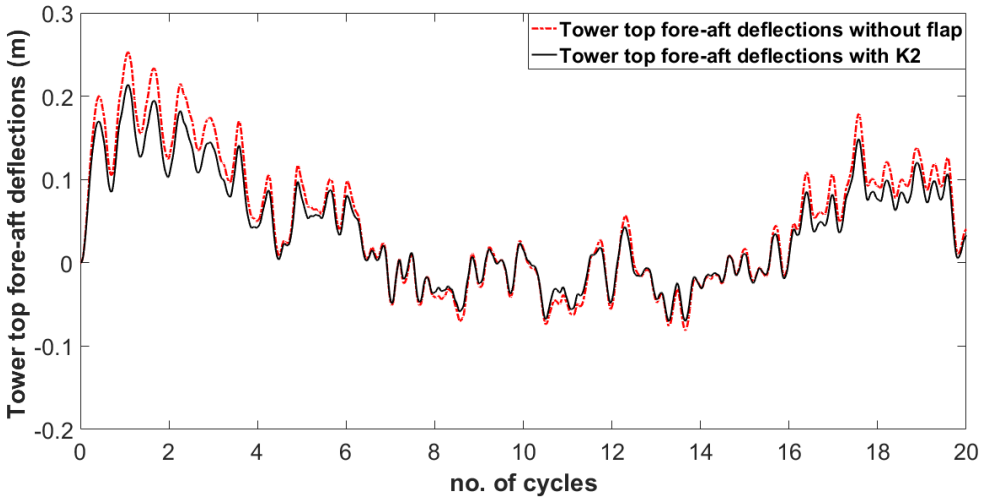

(b) Tower top fore-aft deflection

Figure 10: Time simulation for blade tip deflection and tower top fore-aft deflection and the wind turbine without and with flap actuated by controller K2, in a flow velocity of 14 m/s and turbulence intensity of 17.5%.

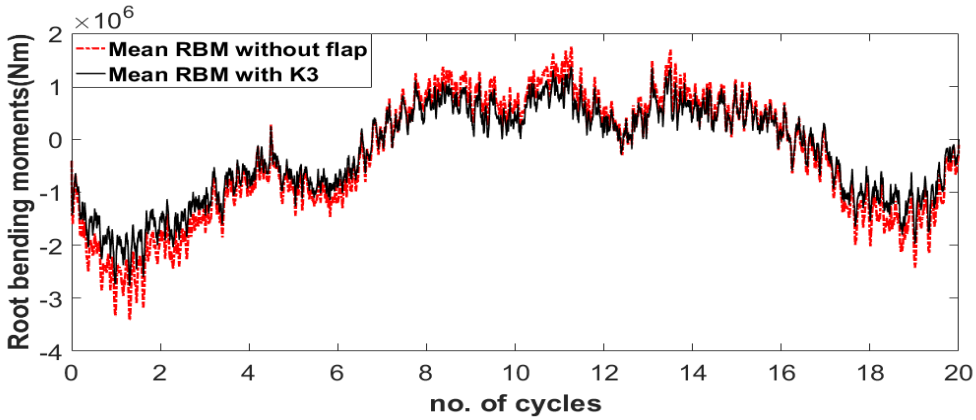

(a) Blade flapwaise RBM

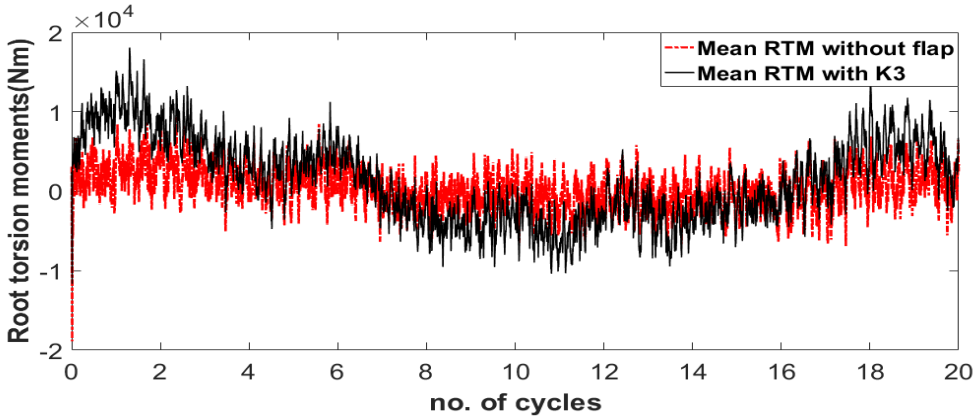

(b) Blade RTM

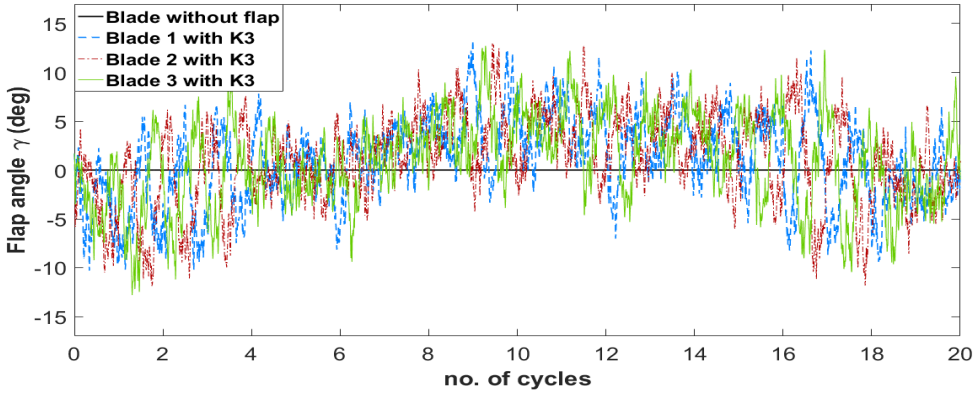

(c) Flap deflection angle

Figure 11: Time simulation for flapwise RBM, blade RTM and flap angle of wind turbine blades without and with flap actuated by controller K3, in a flow velocity of 14 m/s and turbulence intensity of 17.5%.

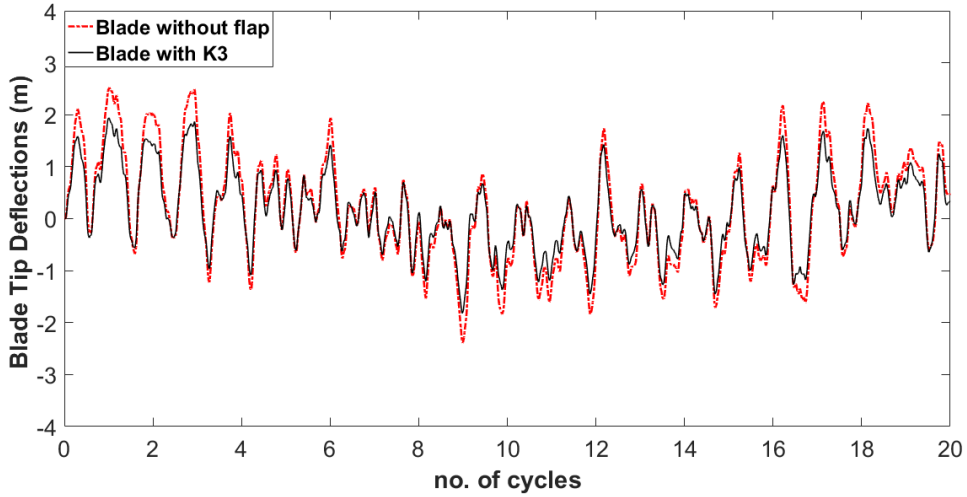

(a) Blade tip deflection

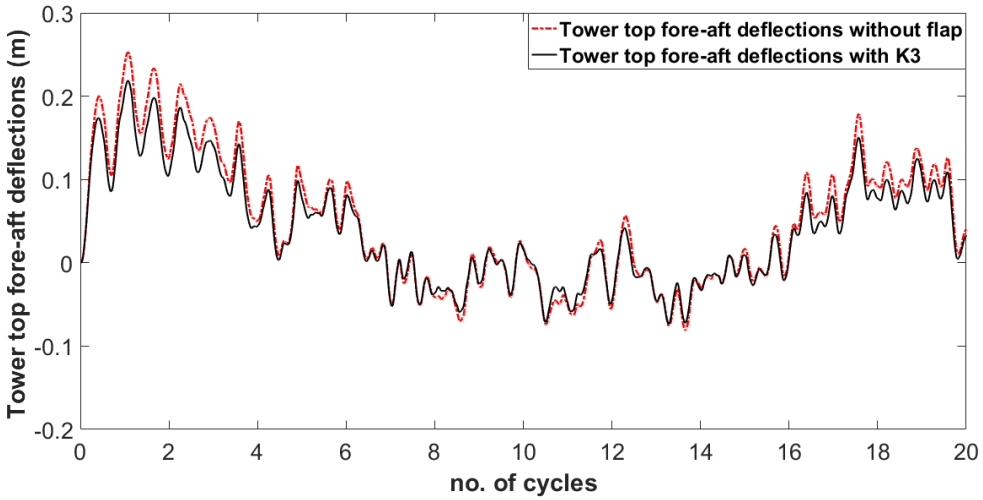

(b) Tower top fore-aft deflection

Figure 12: Time simulation for blade tip deflection and tower top fore-aft deflection of the wind turbine without and with flap actuated by controller K3, in a flow velocity of 14 m/s and turbulence intensity of 17.5%.

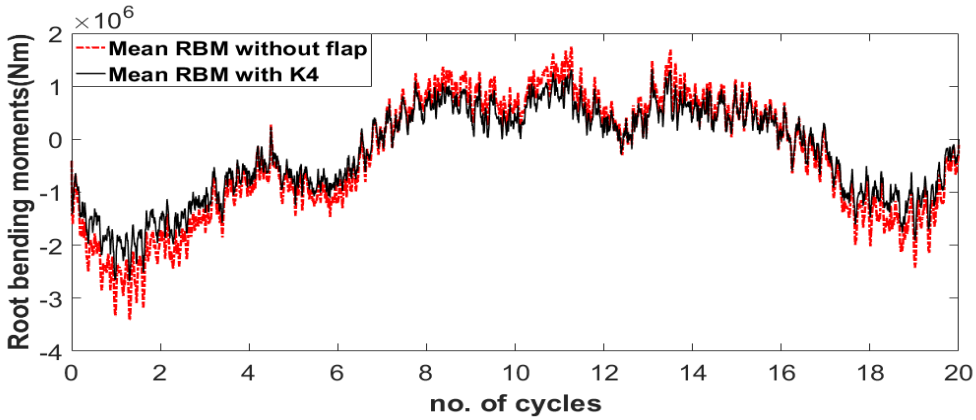

(a) Blade flapwaise RBM

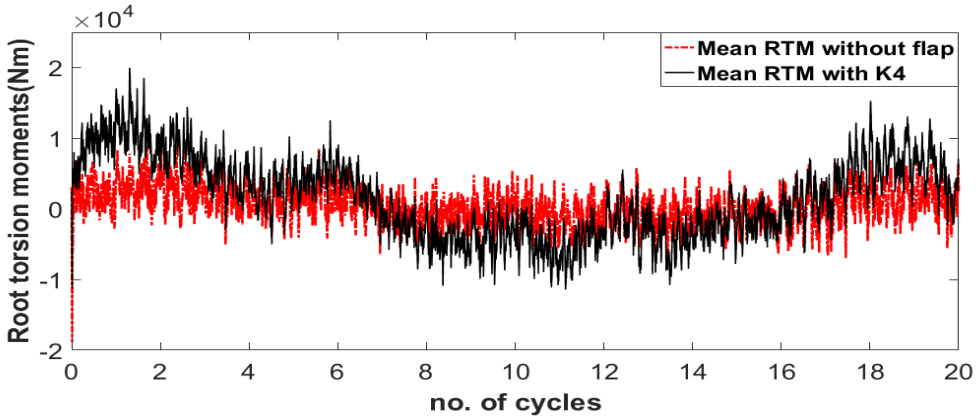

(b) Blade RTM

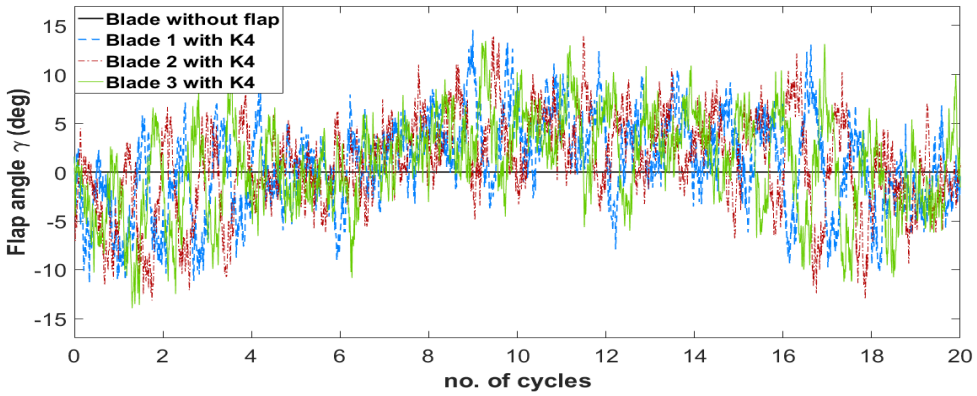

(c) Flap deflection angle

Figure 13: Time simulation for flapwise RBM, blade RTM and flap angle of wind turbine blades without and with flap actuated by controller K4, in a flow velocity of 14 m/s and turbulence intensity of 17.5%.

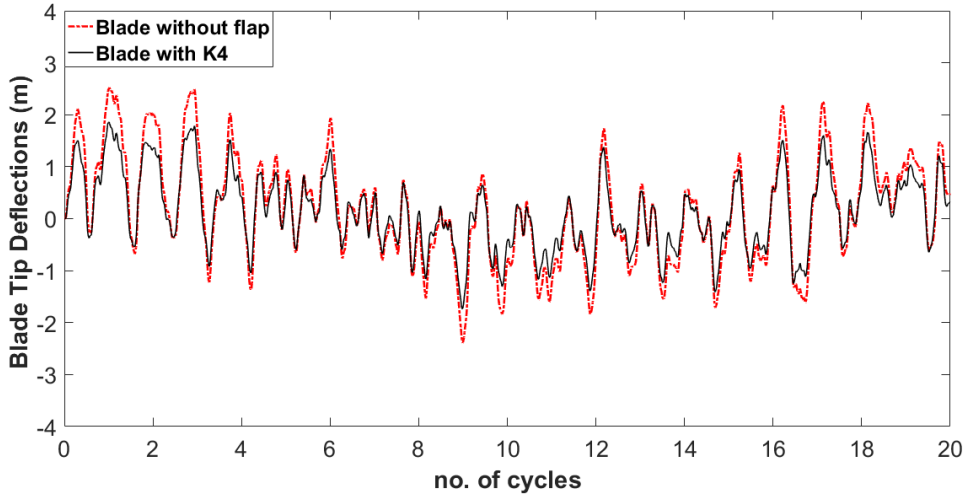

(a) Blade tip deflection

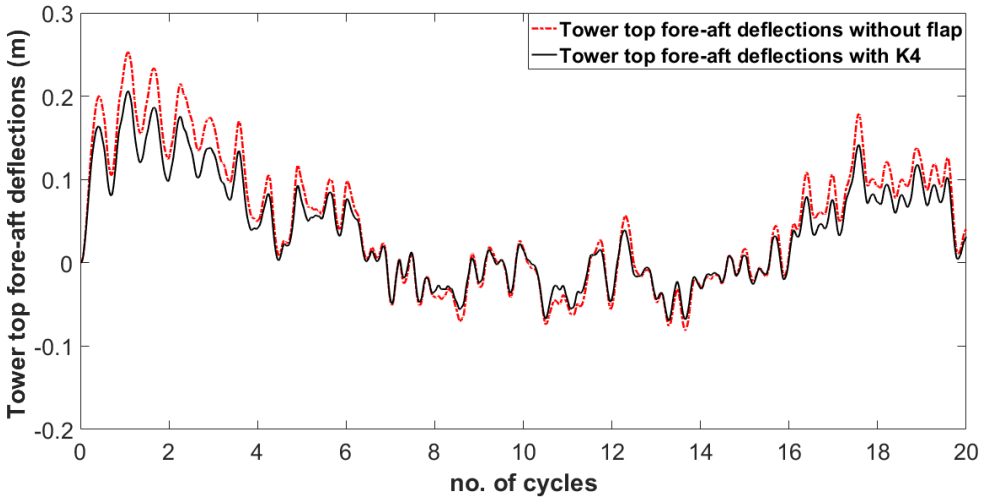

(b) Tower top fore-aft deflection

Figure 14: Time simulation for blade tip deflection and tower top fore-aft deflection of the wind turbine without and with flap actuated by controller K4, in a flow velocity of 14 m/s and turbulence intensity of 17.5%.

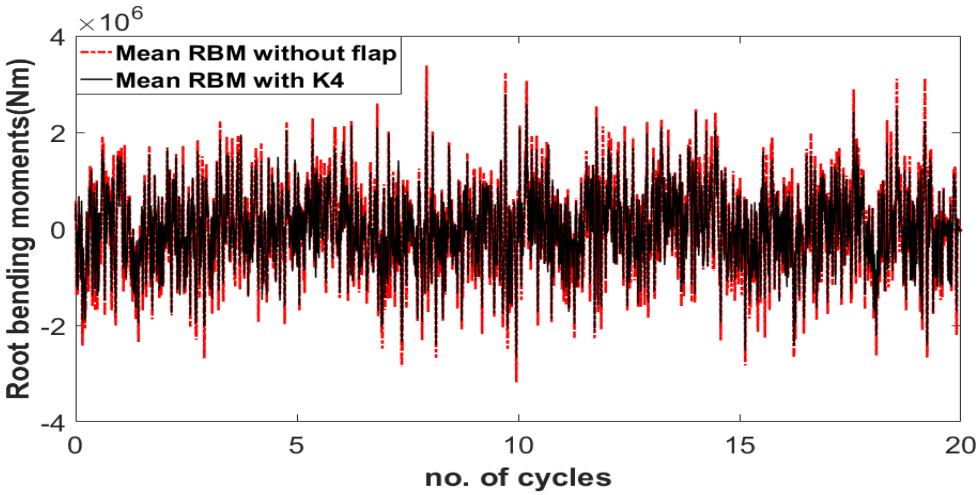

(a) Blade flapwaise RBM

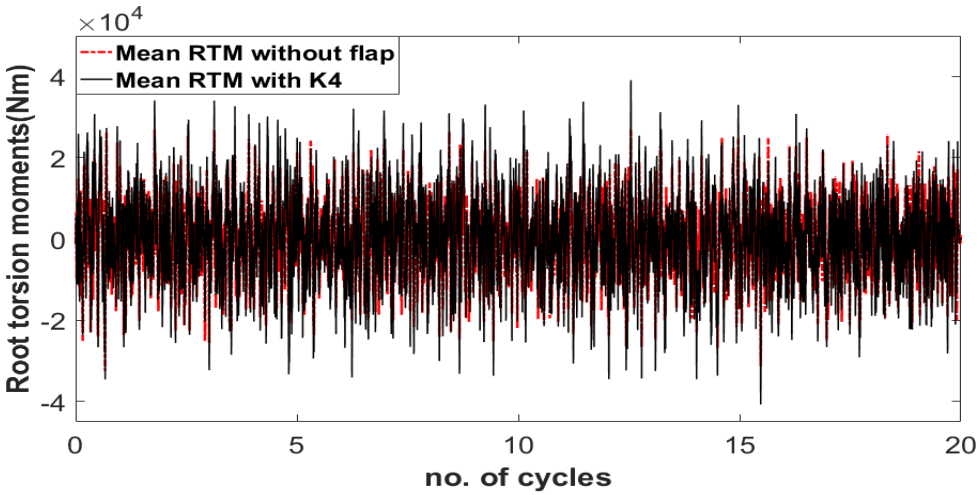

(b) Blade RTM

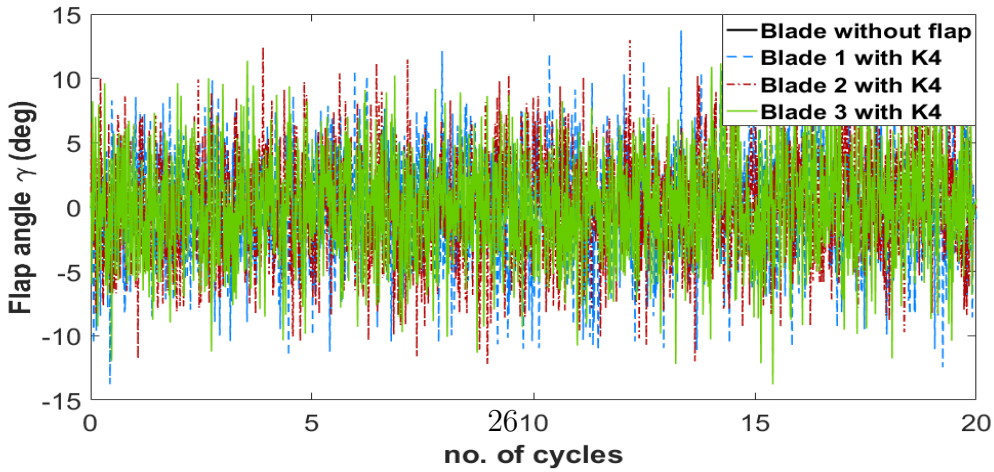

(c) Flap deflection angle

Figure 15: Time simulation for flapwise RBM, blade RTM and flap angle of wind turbine blades without and with flap actuated by controller K4, in DLC 1.3 with mean wind speed of 14 m/s and turbulence intensity of 17.5%.

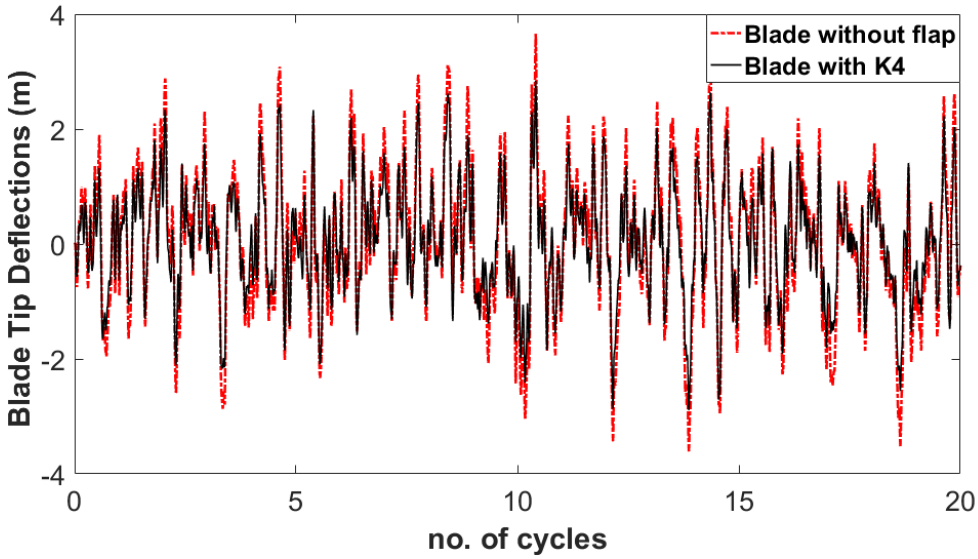

(a) Blade tip deflection

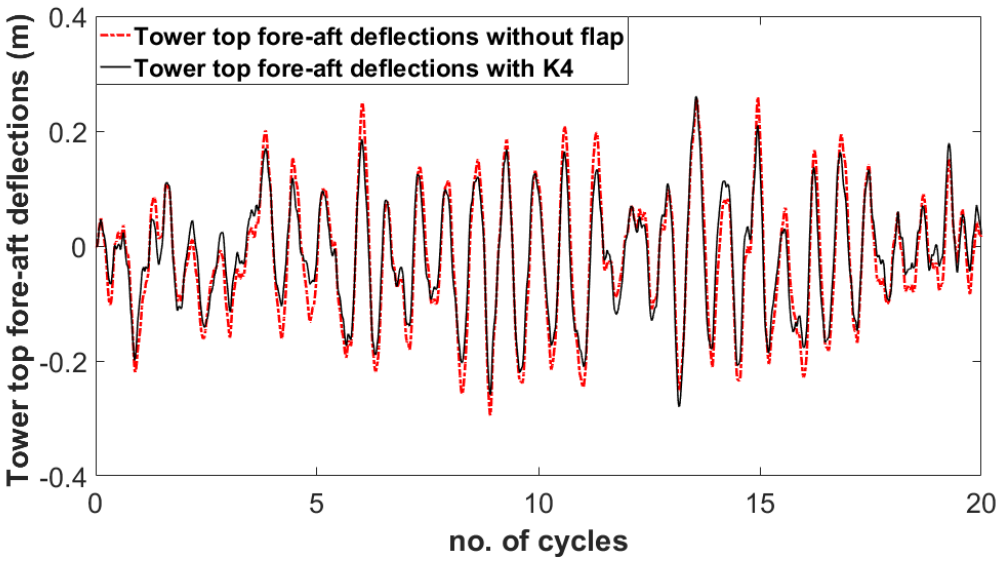

(b) Tower top fore-aft deflection

Figure 16: Time simulation for blade tip deflection and tower top fore-aft deflection of the wind turbine without and with flap actuated by controller K4, in DLC 1.3 with mean wind speed of 14 m/s and turbulence intensity of 17.5%.

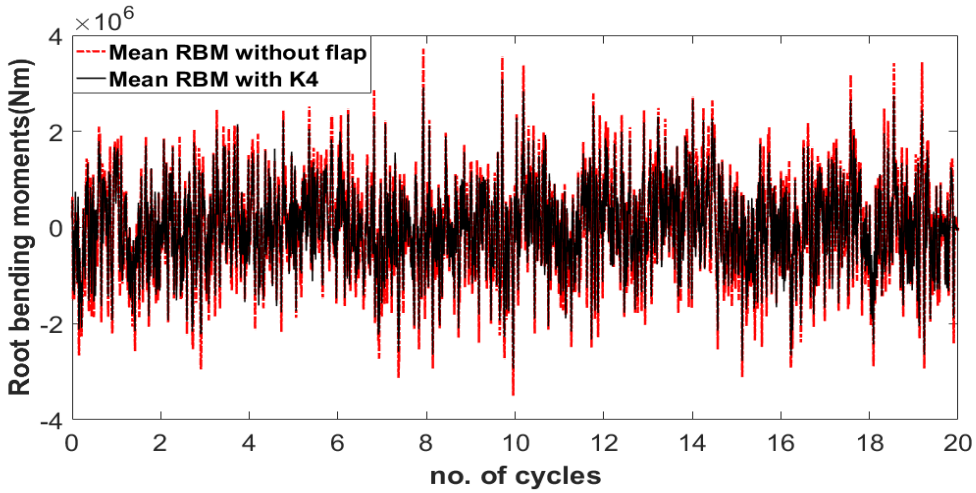

(a) Blade flapwaise RBM

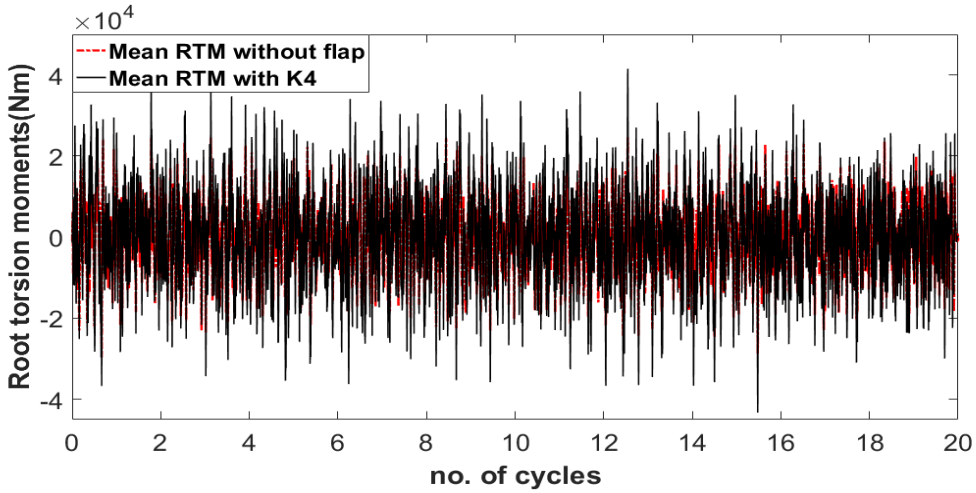

(b) Blade RTM

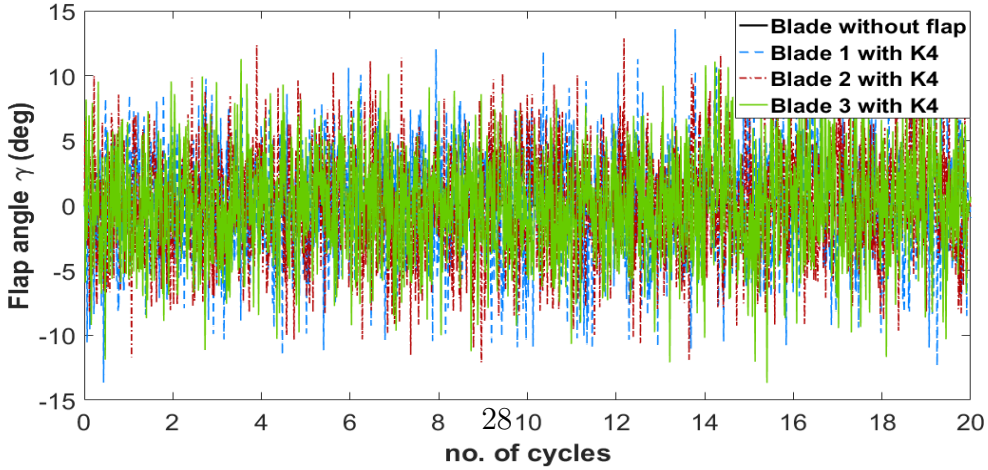

(c) Flap deflection angle

Figure 17: Time simulation for flapwise RBM, blade RTM and flap angle of wind turbine blades without and with flap actuated by controller K4, in DLC 6.1 with mean wind speed of 14 m/s and turbulence intensity of 17.5%.

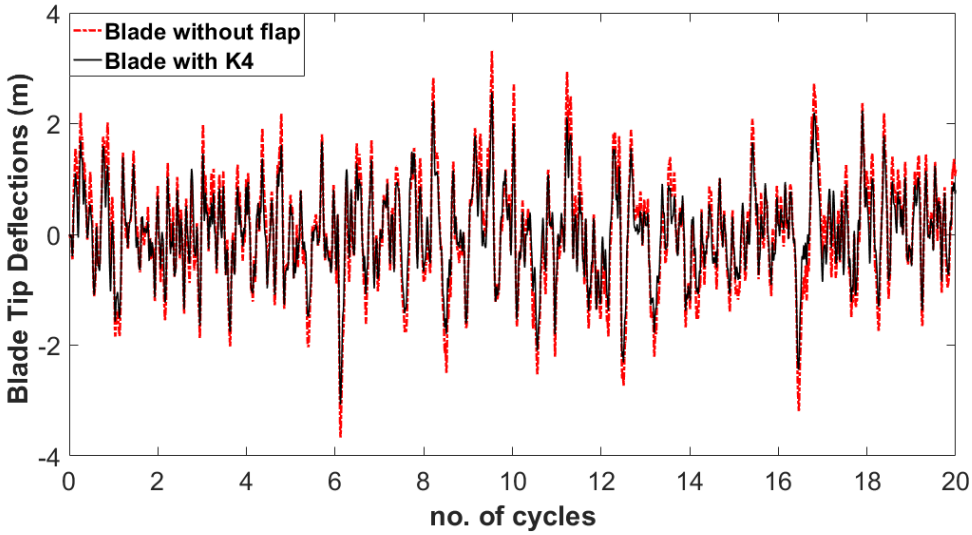

(a) Blade tip deflection

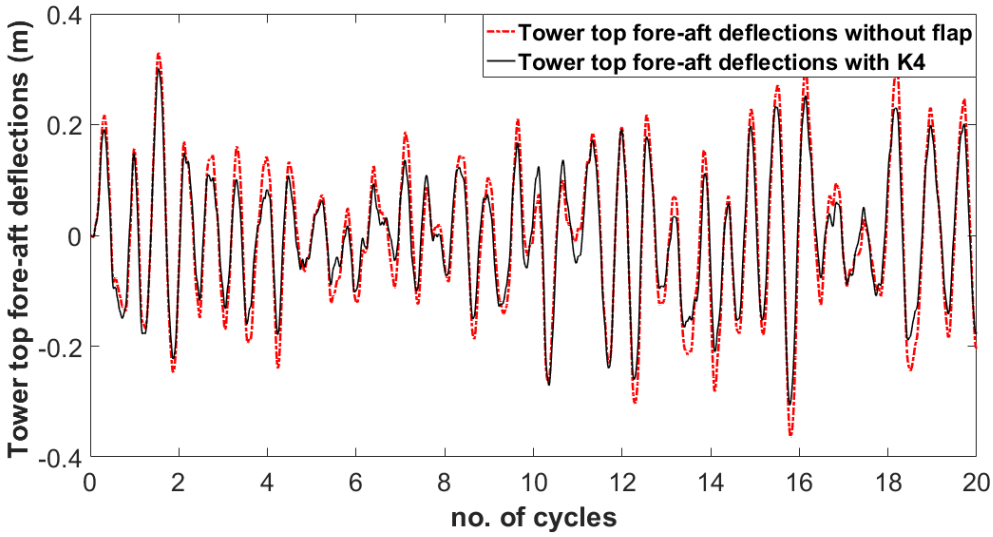

(b) Tower top fore-aft deflection

Figure 18: Time simulation for blade tip deflection and tower top fore-aft deflection of the wind turbine without and with flap actuated by controller K4, in DLC 6.1 with mean wind speed of 14 m/s and turbulence intensity of 17.5%.

Table 3: Closed-loop alleviation of blade loads under the case of DLCs 1.3 and 6.1 with flaps actuated by controllers K1, K2, K3 and K4. Negative sign implies an increase. The abbreviations are: rms (root-mean-square), RBM (root-bending moment), RTM (root-torsion moment) BTD (balde tip deflection), rd (reduction), TTFAD (tower top fore-aft deflection)

Controller name	%rd RMS RBM	%rd max BTD	max γ (°)	%rd RMS RTM	%rd RMS TTFAD
K1(DLC1.3)	12.84	9.51	9.83	-34.71	11.57
K2(DLC1.3)	14.68	12.31	10.57	-43.68	13.24
K3(DLC1.3)	17.59	15.84	11.21	-52.45	15.65
K4(DLC1.3)	19.81	17.67	14.62	-59.63	17.82
K1(DLC6.1)	11.84	10.64	12.37	-38.94	12.34
K2(DLC6.1)	13.26	13.85	12.89	-44.36	14.15
K3(DLC6.1)	17.31	17.47	13.49	-53.68	16.62
K4(DLC6.1)	18.86	18.32	14.62	-64.75	18.73

been designed for the trailing-edge flap based on a single rotating blade model for passive alleviation of flapwise RBM. Simulation results based on the three-dimensional wind turbine model showed that marked reductions of flapwise RBM, blade tip deflection and tower top fore-aft deflection can be achieved for the turbulence in three cases of DLCs and gust excitations. The maximum flap angle is kept within $\pm 15^\circ$ without enforcing constraints on flap deflection limits, which is commonly adopted in active control method to restrict flap angles. Compared with active control methods, the mechanical controller is more energy-efficient, easy to implement and more reliable.

ACKNOWLEDGEMENT

This work is funded by an International Partnership Fund from the University of Warwick and a start-up grant from Nanyang Technological University. The authors had useful talk with Dr. Yinan Wang.

REFERENCES

[1] J. H. Laks, L. Y. Pao, A. D. Wright, Control of wind turbines: Past, present, and future, in: 2009 american control conference, IEEE, 2009, pp. 2096–2103.

[2] M. A. Lackner, G. A. M. van Kuik, A comparison of smart rotor control approaches using trailing edge flaps and individual pitch control, Wind Energy: An International Journal for Progress and Applications in Wind Power Conversion Technology 13 (2-3) (2010) 117–134.

[3] M. O. L. Hansen, J. N. Sørensen, S. Voutsinas, N. Sørensen, H. A. Madsen, State of the art in wind turbine aerodynamics and aeroelasticity, Progress in aerospace sciences 42 (4) (2006) 285–330.

[4] J. E. Herencia, P. M. Weaver, M. I. Friswell, Morphing wing design via aeroelastic tailoring, in: Proceedings of 48th AIAA/ASME/ASCE/AHS/ASC Structures, Structural Dynamic and Materials Conference, 2007, p. 2214.

[5] C. Bottasso, F. Campagnolo, A. Croce, C. Tibaldi, Optimization-based study of bend-twist coupled rotor blades for passive and integrated passive/active load alleviation, Wind Energy 16 (8) (2013) 1149–1166.

[6] T. K. Barlas, G. A. M. van Kuik, Review of state of the art in smart rotor control research for wind turbines, Progress in Aerospace Sciences 46 (1) (2010) 1–27.

[7] C. Plumley, W. Leithead, P. Jamieson, E. Bossanyi, M. Graham, Comparison of individual pitch and smart rotor control strategies for load reduction, in: Journal of Physics: Conference Series, Vol. 524, IOP Publishing, 2014, p. 012054.

[8] E. A. Bossanyi, Individual blade pitch control for load reduction, Wind Energy: An International Journal for Progress and Applications in Wind Power Conversion Technology 6 (2) (2003) 119–128.

[9] L. Bergami, N. K. Poulsen, A smart rotor configuration with linear quadratic control of adaptive trailing edge flaps for active load alleviation, Wind Energy 18 (4) (2015) 625–641.

[10] T. K. Barlas, W. van Wingerden, A. W. Hulskamp, G. A. M. van Kuik, H. E. N. Bersee, Smart dynamic rotor control using active flaps on a small-scale wind turbine: aeroelastic modeling and comparison with wind tunnel measurements, Wind Energy 16 (8) (2013) 1287–1301.

[11] D. Castaignet, I. Couchman, N. K. Poulsen, T. Buhl, J. J. Wedel-Heinen, Frequency-weighted model predictive control of trailing edge flaps on a wind turbine blade, IEEE Transactions on Control Systems Technology 21 (4) (2013) 1105–1116.

[12] T. K. Barlas, G. J. Van Der Veen, G. A. M. Van Kuik, Model predictive control for wind turbines with distributed active flaps: incorporating inflow signals and actuator constraints, Wind Energy 15 (5) (2012) 757–771.

[13] B. F. Ng, R. Palacios, J. M. R. Graham, Model-based aeroelastic analysis and blade load alleviation of offshore wind turbines, International Journal of Control 90 (1) (2017) 15–36.

[14] B. F. Ng, H. Hesse, E. C. Kerrigan, R. Palacios, J. M. R. Graham, Efficient aeroservoelastic modeling and control using trailing-edge flaps of wind turbines, in: 2014 UKACC International Conference on Control (CONTROL), IEEE, 2014, pp. 1–6.

[15] D. Wilson, T. Barlas, D. Berg, G. A. M. van Kuik, B. Resor, Active aerodynamic blade distributed flap control design proceedure for load reduction on the upwind 5mw wind turbine, in: 48th AIAA Aerospace Sciences Meeting Including the New Horizons Forum and Aerospace Exposition, 2010, p. 254.

[16] A. W. Hulskamp, J. W. Van Wingerden, T. Barlas, H. Champliaud, G. A. M. Van Kuik, H. E. Bersee, M. Verhaegen, Design of a scaled wind turbine with a smart rotor for dynamic load control experiments, Wind Energy 14 (3) (2011) 339–354.

[17] M. C. Smith, Synthesis of mechanical networks: the inerter, IEEE Transactions on Automatic Control 47 (10) (2002) 1648–1662.

[18] M. Z. Q. Chen, M. C. Smith, Restricted complexity network realizations for passive mechanical control, IEEE Transactions on Automatic Control 54 (10) (2009) 2290–2301.

[19] K. Wang, M. Z. Q. Chen, C. Li, G. Chen, Passive controller realization of a biquadratic impedance with double poles and zeros as a seven-element series-parallel network for effective mechanical control, IEEE Transactions on Automatic Control 63 (9) (2018) 3010–3015.

[20] M. Z. Q. Chen, M. C. Smith, A note on tests for positive-real functions, IEEE Transactions on Automatic Control 54 (2) (2009) 390–393.

[21] M. Z. Q. Chen, C. Papageorgiou, F. Scheibe, F. C. Wang, M. C. Smith, The missing mechanical circuit element, IEEE Circuits and Systems Magazine 9 (1) (2009) 10–26.

[22] J. M. R. Graham, D. J. N. Limebeer, X. Zhao, Aeroelastic modelling of long-span suspension bridges, IFAC Proceedings Volumes 44 (1) (2011) 9212–9217.

[23] D. J. N. Limebeer, J. M. R. Graham, X. Zhao, Buffet suppression in long-span suspension bridges, Annual Reviews in Control 35 (2) (2011) 235–246.

[24] X. Zhao, K. Gouder, J. M. R. Graham, D. J. N. Limebeer, Buffet loading, dynamic response and aerodynamic control of a suspension bridge in a turbulent wind, Journal of Fluids and Structures 62 (2016) 384–412.

[25] J. M. R. Graham, D. J. N. Limebeer, X. Zhao, Aeroelastic control of long-span suspension bridges, Journal of Applied Mechanics 78 (4) (2011) 041018.1–041018.12.

[26] K. N. Bakis, M. Massaro, M. S. Williams, D. J. N. Limebeer, Aeroelastic control of long-span suspension bridges with controllable winglets, Structural Control and Health Monitoring 23 (12) (2016) 1417–1441.

[27] K. Gouder, X. Zhao, D. J. N. Limebeer, J. M. R. Graham, Experimental aerodynamic control of a long-span suspension bridge section using leading-and trailing-edge control surfaces, IEEE Transactions on Control Systems Technology 24 (4) (2016) 1441–1453.

[28] Y. Hu, J. Wang, M. Z. Q. Chen, Z. Li, Y. Sun, Load mitigation for a barge-type floating offshore wind turbine via inerter-based passive structural control, Engineering Structures 177 (2018) 198–209.

[29] Y. Hu, M. Z. Q. Chen, Inerter-based passive structural control for load mitigation of wind turbines, in: 2017 29th Chinese Control And Decision Conference (CCDC), IEEE, 2017, pp. 3056–3061.

[30] J. Jonkman, S. Butterfield, W. Musial, G. Scott, Definition of a 5-mw reference wind turbine for offshore system development, National Renewable Energy Laboratory, Golden, CO, Technical Report No. NREL/TP-500-38060.

[31] B. F. Ng, R. Palacios, E. C. Kerrigan, J. M. R. Graham, H. Hesse, Aerodynamic load control in horizontal axis wind turbines with combined aeroelastic tailoring and trailing-edge flaps, Wind Energy 19 (2) (2016) 243–263.

[32] J. Katz, A. Plotkin, Low-speed aerodynamics, Vol. 13, Cambridge university press, 2001.

[33] M. Géradin, A. Cardona, Flexible multibody dynamics: a finite element approach, John Wiley Chichester, England; New York, USA, 2001.

[34] J. Murua, R. Palacios, J. M. R. Graham, Applications of the unsteady vortex-lattice method in aircraft aeroelasticity and flight dynamics, Progress in Aerospace Sciences 55 (2012) 46–72.

[35] J. J. Chattot, Helicoidal vortex model for wind turbine aeroelastic simulation, Computers & Structures 85 (11-14) (2007) 1072–1079.

[36] F. J. Simoes, J. M. R. Graham, Application of a free vortex wake model to a horizontal axis wind turbine, Journal of Wind Engineering and Industrial Aerodynamics 39 (1-3) (1992) 129–138.

[37] I. E. Commission, et al., Iec 61400-1: Wind turbines part 1: Design requirements, International Electrotechnical Commission.